Design and Demonstration of a 100 kW High-Frequency Matrix Core Transformer for More Electric Aircraft Power Distribution

Zhe Zhao, *Graduate Student Member, IEEE*, Yuheng Wu, *Student Member, IEEE*, Fei Diao, *Graduate Student Member, IEEE*, Nan Lin, *Graduate Student Member, IEEE*, Xinyuan Du, *Student Member*, Yue Zhao, *Senior Member, IEEE*, and Guangqi Zhu, *Member, IEEE*

***Abstract*—The rapid development of more electric aircraft (MEA) raises the demand of high-power converters with significant weight and volume reduction for onboard power distribution. The isolated DC/DC converter using the medium-frequency transformer (MFT) is a feasible solution. To design an MFT with improved electromagnetic and thermal performance, a matrix core transformer (MCT) architecture is proposed with accurate models in this paper. With superior heat dissipation ability, the high current windings can be effectively cooled with both natural and forced air convection. In addition, an optimization methodology for MCT design is presented. As a result, the prototype of a 100 kW, 50 kHz MCT with an additive manufactured bobbin is built. The results of both finite element analysis (FEA) simulation and experimental study in a full power dual active bridge with the MCT prototype are presented to verify the theoretical design. The power density and efficiency of the MCT reach to 17.7 kW/L and 99.63%, respectively.**

***Index Terms*—Medium-frequency transformer, more electric aircraft (MEA), power distribution.**

I. Introduction

As a promising solution for the future commercial aircrafts, the more electric aircraft (MEA) gets much attention due to its ability to achieve higher efficiency and lower weight [1]. In addition, MEA is an environmental-friendly solution with lower fuel consumption and less greenhouse gas (GHG) emission. An example of power distribution system in MEA is shown in Fig. 1, in which the HVDC bus is used for delivering the power. There are several commercial aircrafts available with more electric features, such as the Boeing 787 and Airbus A380, where engines are directly coupled with the generators to lower power losses in the transmission. However, the need of power level on MEA is still rapidly increasing beyond 1 MW [2]. To meet this need, the high power converters for power distribution and motor drives with significantly higher specific power (kW/kg) and volumetric power density (kW/L) are still needed to be developed. Thanks to the advancement of wide bandgap semiconductor technology, silicon carbide (SiC) devices with high blocking voltage capabilities, e.g., 10 kV [3] and 15 kV [4], and switching frequency lead to the rapidly increased interests for high power converters in the medium voltage (MV) application [5-7]. The concept of solid-state transformer (SST) is proposed as a disruptive solution for power conversion with galvanic isolation [8]. The SST replaced the bulky line-frequency transformer with the medium-frequency transformer (MFT), which reduces the size and weight of the conversion system significantly. There are several high-power SST designs reported in the existing literature, such as a 10 MW, 1 kHz SST setup presented in [9]. Both the high-power density and high-power operation capability advance the development of SST for aerospace applications [10]-[12].

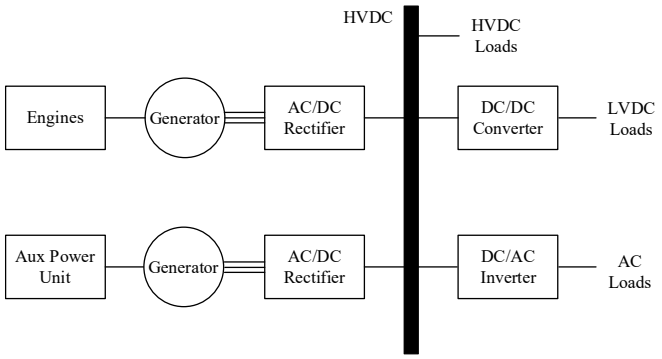

Fig. 1. Electrical power distribution system of MEA.

The most commonly using building block in the SST is the dual active bridge (DAB) converter, whose topology, typical operating waveforms, and equivalent circuit are illustrated in Fig. 2 [13]. The bidirectional power delivery is controlled by adjusting the phase shift between the two H-bridges. The MFT not only provides the galvanic insulation for the converter, but also is indispensable for delivering power, especially the leakage inductance of the MFT is an essential component for power level control and soft switching realization [14]. Even though an external inductor connected in series with the transformer winding can be an alternative, the integrated solution, i.e., using an optimized leakage inductance of the MFT, can be a better solution to get rid of the need for external inductor and increase the power density. The methods to design and estimate the leakage inductance are discussed in [15]-[17] and the comparison among them in terms of the accuracy and

This work was supported by in part by the U.S. National Science Foundation (NSF) Center on Grid Connected Advanced Power Electronic Systems (GRAPES) under Grant 1939144 and also by the NSF Engineering Research Center for Power Optimization of Electro Thermal Systems (POETS) with cooperative agreement EEC-1449548.

Z. Zhao, Y. Wu, F. Diao, N. Lin, X. Du, F. Guo, and Y. Zhao are with Power Electronic Systems Laboratory, University of Arkansas, Fayetteville, AR, USA (e-mail: zhezhao@uark.edu; yuhengwu@uark.edu; feidiao@uark.edu; nl005@uark.edu; xd006@uark.edu; fengg@uark.edu; yuezhao@uark.edu).

G. Zhu is with Research Labs, Eaton, Menomonee Falls, WI, USA (e-mail: GuangqiZhu@eaton.com).

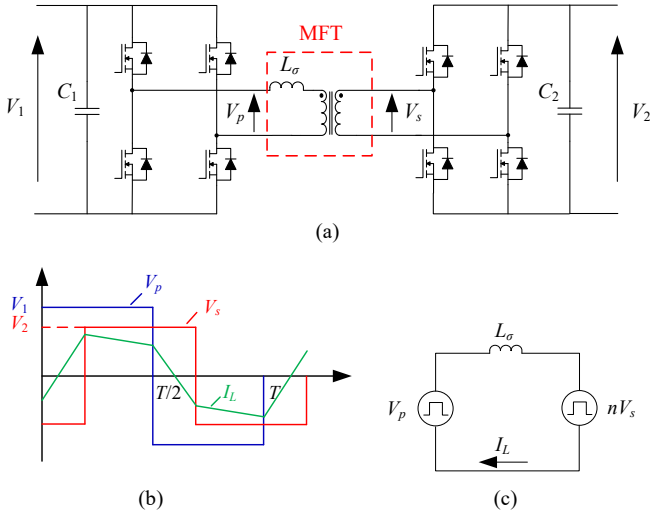

Fig. 2. (a) The topology, (b) typical operation waveforms, and (c) equivalent circuit of DAB.

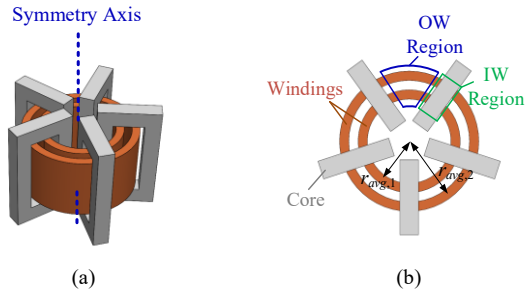

Fig. 3. (a) The structure of MCT and (b) the top view.

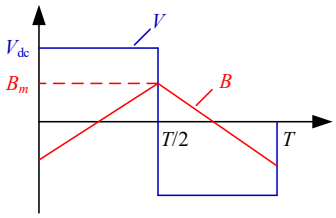

Fig. 4. Applied voltage and excited flux density of the MFT in a DAB converter.

computational burden is presented in [18].

the core window (OW) instead of inside the core window (IW), which increases the heat dissipation capability. Analytical models of MCT are introduced in this section, which is critical for the MCT design and optimization to be presented later.

A. Core Loss Models

Soft magnetic materials are widely used in transformer design, and they are classified as ferrites, laminated iron alloys, iron powder, amorphous alloys and nanocrystalline materials [25]. Even though the saturation flux density of nanocrystalline cores can achieve 1.5 T and is considered has the lowest core loss in the medium frequency range, the ferrites cores are preferred as the frequency increases since the nanocrystalline cores are tape-wound with conductive ribbon, which worsens the eddy current loss significantly [26], [27]. Besides, the prices of ferrite cores are much lower than nanocrystalline cores, thus the ferrite cores are selected for this 50 kHz application.

To design the high power MFTs for MEA applications, it is critical to achieve not only the high efficiency and power density, but also the excellent heat dissipation and voltage insulation. There are several publications focus on the MFTs design to achieve one or more of these design requirements. A 99% efficient 25 kW MFT with vacuum pressure potting technology was presented in [19] for a 7 kV-to-400 V insulation design. A 100 kW, 10 kHz MFT prototype was setup in [20] with accurate leakage and thermal models. A 200 kVA 10kHz MFT presented in [21] used nanocrystalline core for lower core loss, and similar work in [22] increases the frequency to 15 kHz with parallel-concentric winding structure. An ultra-high-power density of 32.7 kW/L was achieved for the MFT illustrated in [23] for 166 kW power level application with liquid cooling. The matrix core transformer (MCT) is proved to work for a 25 kW, 50 kHz SST, and the analysis of parasitic parameters of MCT was focused for resonant frequency estimation in [24]. To achieve higher power density, further increase the switching frequency can be a solution, which however is challenging to realize for the 100 kW+ power rating. In this work, the design of a 100 kW, 50 kHz MCT, especially its thermal model and optimization algorithm, is proposed, which is lacking in existing literature. The experimental results of the prototype of the optimal MCT design verify the excellent thermal performance of this structure.

The paper is organized as follows. The electromagnetic and thermal models and design considerations are introduced in Section II. Section III discusses the optimization methodology of MCT, presents the optimal MCT design with finite element analysis (FEA) simulation. The experimental results with electrical and thermal characteristics are given in Section IV. Finally, the conclusions are presented in Section V.

II. Modeling and Design Considerations of MCT

The structure of proposed MCT is shown in Fig. 3, where the MCT has a rotational symmetry in the center, leading to a circular winding structure. This design can expose much more core surface area and provide an effective air flow channel between the windings. The windings are mainly located outside

The core loss is made up with classical eddy current loss, excess eddy current loss and hysteresis loss [28]. Steinmetz first proposed the classic core loss model, which expresses the core loss as a function of frequency and flux density [29]. Then several works modified the original Steinmetz equation to reduce the estimation error [30]-[32]. Considering the tradeoff between the computational burden and accuracy, the improved generalized Steinmetz's equation (IGSE) is used and the core loss per volume P_c can be calculated as

$$P_c = \frac{1}{T}\int_0^T k_i \left|\frac{\mathrm{d}B(t)}{\mathrm{d}t}\right| (\Delta B)^{\beta-\alpha}\,\mathrm{d}t \tag{1}$$

is used,

$$K_i = \frac{K}{2^{\beta-1}\pi^{\alpha-1}\int_0^{2\pi}|\cos\theta|^{\beta}\mathrm{d}\theta}, \tag{2}$$

where K, α, and β are the Steinmetz coefficients. A general

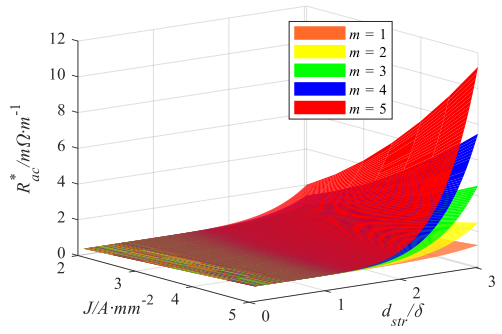

Fig. 5. A 3-D plot of R^*_{ac} as functions of d_{str} and J with the number of layers m varying from 1 to 5 for square litz wire.

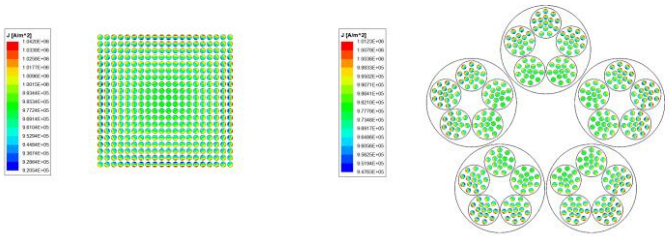

(a)

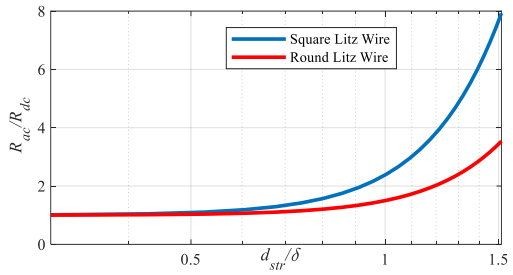

(b)

Fig. 6. Comparison of square and round litz wire on (a) current distribution and (b) ac resistance.

closed-form expression for core loss estimation with variable duty ratio and phase shift for DAB converter is presented in [33], where (1) is simplified as

$$P_c = 2^{\alpha+\beta} K_i f^{\alpha} B_m^{\beta} \tag{3}$$

for traditional single-phase shift (SPS) modulation with the square voltage excitation and triangle flux density waveform depicted in Fig. 4, where B_m is the peak flux density.

B. Winding Loss Models and Litz Wire Selection

Besides the resistive loss caused by the high transformer current, the winding loss worsens as the frequency increases due to the skin effect and proximity effect. The skin depth δ is a crucial parameter to represent the uneven current distribution in the conductors, which is expressed as

$$\delta = \frac{1}{\sqrt{\pi f \mu \sigma}}, \tag{4}$$

where f is the frequency, μ is the permeability, and σ is the conductivity of the conductor. The Dowell model [34] is a remarkable work to estimate the winding loss for foil winding with the skin and proximity factors defined as

$$\xi_S = \frac{\sinh 2\Delta + \sin 2\Delta}{\cosh 2\Delta - \cos 2\Delta}, \tag{5}$$

$$\xi_P = \frac{\sinh \Delta - \sin \Delta}{\cosh \Delta + \cos \Delta}, \tag{6}$$

respectively, where Δ is the ratio of the layer thickness to the skin depth δ, and the ratio of ac resistance to dc resistance F_r is calculated as

$$F_r = \frac{R_{\mathrm{ac}}}{R_{\mathrm{dc}}} = \Delta\left[\xi_S + \frac{2}{3}\left(m^2 - 1\right)\xi_P\right], \tag{7}$$

where m is the number of winding layers.

The litz wire with multiple individually insulated conductor strands uses complex twisting to mitigate the ac winding losses. The strand diameter d_{str} should be lower than the skin depth δ. For a fixed winding current I, the relationship between the strand diameter d_{str} and the number of strands k is as

$$k = \frac{A}{\frac{\pi}{4} d_{str}^2} = \frac{I}{\frac{\pi}{4} d_{str}^2 J}, \tag{8}$$

where A is the total cross-section area of the litz wire winding, and J is the average current density. The approximate Dowell's equation for square litz wire with $d_{str} < 2\delta$ is given in [35] as

$$F_r = \frac{R_{\mathrm{ac}}}{R_{\mathrm{dc}}} \approx 1 + \frac{5m^2 k - 1}{45} \Delta_{str}^4, \tag{9}$$

where and Δ_{str} is the normalized value of Δ for one strand, which is expressed as

$$\Delta_{str} = \left(\frac{\pi}{4}\right)^{0.75} \frac{d_{str}}{\delta} \sqrt{\frac{d_{str}}{k\left(d_{str} + p\right)}}, \tag{10}$$

where p is the distance between adjacent strands in one layer. The dc resistance R_{dc} can be calculated as

$$R_{\mathrm{dc}} = \frac{L}{\sigma A}, \tag{11}$$

where L is the length of the winding, and is expressed as

$$L = 2\pi N r_{avg} \tag{12}$$

for MCT, N is the number of turns, and r_{avg} is the average radius of the winding. The ac resistance can be obtained by substituting (8), (10) and (11) into (9) as

$$R_{\mathrm{ac}} = \frac{L}{\sigma \frac{I}{J}}\left[1 + \frac{\pi^4}{46080} \cdot \frac{\left(20m^2 I - \pi d_{str}^2 J\right) d_{str}^8 J}{I^2 \left(d_{str} + p\right)^2 \delta^4}\right]. \tag{13}$$

As an example, Fig. 5 shows the ac resistances per meter R_{ac} under different d_{str} and J, where the transformer parameters are set as I = 100 A, f = 50 kHz, and p = 0.04 mm It can be concluded that for high current applications, the strand of litz wire should be selected lower than δ to reduce the ac winding loss, and a large number of winding layers should be avoided to reduce the proximity effect. Thus, the optimal selection of litz wire for the strand diameter and the number of strands is necessary, for each possible current density and frequency [36].

Another consideration for litz wire selection is the shape of the litz wire. Compared to the round litz wire, which is more common with lower cost, the use of square litz wire can achieve higher filling factor. To compare the winding loss of these two

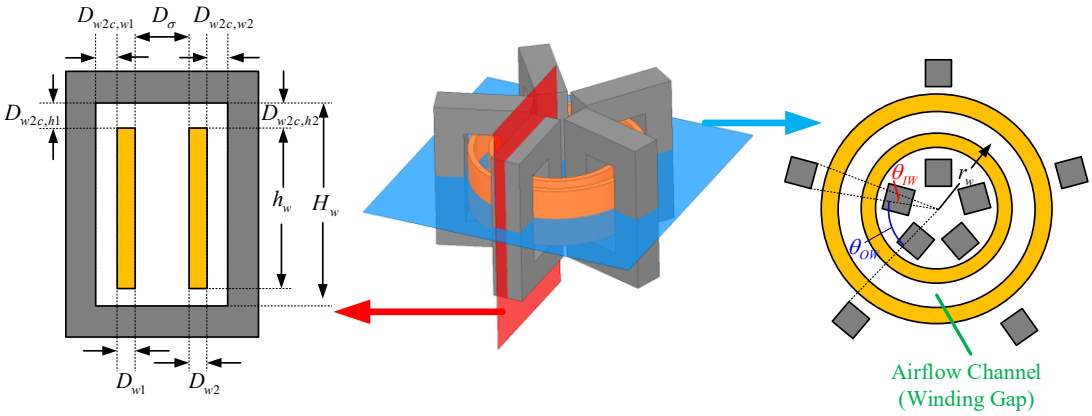

Fig. 7. The cross-section of MCT for leakage inductance calculation.

options, the high frequency effects for both square and round litz wires with the same values of d_{str} and k, i.e., d_{str} = 0.1mm, k = 400, are analyzed by 2-D FEA as shown in Fig. 6. It can be seen that the difference of winding losses can be neglected when $d_{str} < \delta$. As a result, the selection of the shape of litz wires can be made by considering the factors, such as the dimensions of the window area of the core and the cost.

Since the current waveform of the DAB converter is nonsinusoidal as shown Fig. 2, fast Fourier transform (FFT) is used to derive the harmonics in the winding current, such that the winding loss can be calculated as

$$P_w = \sum_{n=1}^{\infty} I_n^2 R_{\mathrm{ac},n}\,, \tag{14}$$

where I_n and $R_{\mathrm{ac},n}$ are the RMS current and ac resistance for the n^{th} order harmonic, respectively.

C. Leakage Inductance Models

In a practical transformer, the nonideal coupling between two windings leads to leakage inductance. A widely used method for the leakage inductance estimation is as [37]

$$L_\sigma = \frac{2W}{I^2} = \frac{\mu_0}{I^2}\int_V H^2 dV\,, \tag{15}$$

where W is the leakage energy in the magnetic field, μ_0 is the permeability of the air, H is the field strength, and V is the total volume. The leakage inductance is closely related to the structure of the transformer, including the geometry of the core and the also geometry of windings. Besides, since the leakage energy is stored not only in the space between the windings, but also in the copper windings, the leakage inductance depends on the frequency due to the skin and proximity effects. However, the frequency-dependent factors can be neglected for medium frequency applications since the variation of leakage inductance can be ignored when the frequency is lower than 100 kHz [37].

To reduce the complexity of (15), using a simplified 2-D transformer model to plot the distribution of magnetomotive force (MMF) is a useful approach [38]. Based on this idea, a simple leakage inductance model [24] for a 1:1 turns-ratio MCT shown in Fig. 7 can be derived as

$$L_\sigma = \mu_0 \frac{2\pi r_w N_1^2}{H_w}\left(\frac{D_{w1}+D_{w2}}{3}+D_\sigma\right), \tag{16}$$

where H_w is the height of window, r_w is the radius of winding window, D_{w1}, D_{w2}, and D_σ are the widths of the primary winding, secondary winding, and winding gap, respectively. However, this approach may have substantial errors for two reasons. First, it neglects the effect of uneven magnetic field distribution due to the leakage flux, and second, it assumes that the windings are fully covered by the cores in MCT. The Rogowski factor [39] can be used to reduce the errors, and the corresponding method is presented as follows.

Since the length of leakage flux is shorter than the core window height at the ends of the windings, the Rogowski factor as

$$K_R = 1 - \frac{1-e^{-\pi h_w/(D_{w1}+D_\sigma+D_{w2})}}{\pi h_w/(D_{w1}+D_\sigma+D_{w2})} \tag{17}$$

is used for correction, where h_w is height of the winding. Then the equivalent height is defined as

$$h_{eq} = \frac{h_w}{K_R}\,. \tag{18}$$

By substituting H_w by h_{eq} into (16), the Rogowski-corrected leakage inductance is as

$$L_{\sigma,\mathrm{Rogowski}} = K_R L_\sigma\,. \tag{19}$$

The accuracy of (19) is proved to be higher than (16) especially with a low value of h_w/H_w [40].

The distribution of the H field of IW and OW in an MCT are compared in Fig. 8. As can be seen, the magnetic field distribution of OW is more scattered than that in IW because of the less influence from cores. Therefore, the leakage inductance increases with a larger OW region. An available approach to consider this effect is to calculate the total leakage inductance as

$$L_\sigma = L_{\sigma,\mathrm{IW}}\cdot l_{\mathrm{IW}} + L_{\sigma,\mathrm{OW}}\cdot l_{\mathrm{OW}}\,, \tag{20}$$

where $L_{\sigma,\mathrm{IW}}$ and $L_{\sigma,\mathrm{OW}}$ are the leakage inductances per unit length for IW and OW windings, respectively, l_{IW} and l_{OW} are the length of IW and OW windings, respectively [18]. However, this method has high computational complexity and hard to use for optimal design of MCT. Therefore, a simplified process is needed. A parameter γ is defined as

$$\gamma = \frac{\theta_{\mathrm{OW}}}{\theta_{\mathrm{OW}}+\theta_{\mathrm{IW}}}\,, \tag{21}$$

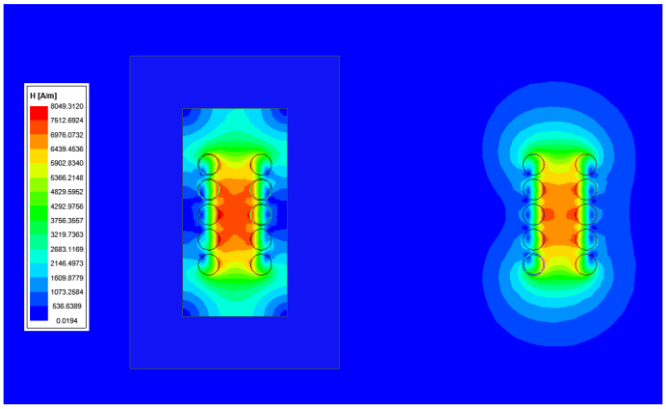

Fig. 8. The simulated H field of IW region (left) and OW region (right). The absence of core in OW region influences the magnetic field distribution and causes the decrease of leakage inductance.

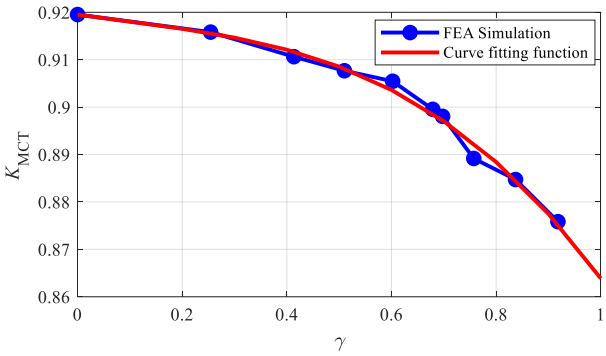

Fig. 9. The plot of K_{MCT} as function of γ based on the 3-D FEA simulation and curve fitting function. The leakage inductance decreases with the OW region occupied more space. The value of K_{MCT} varies around 0.9.

where θ_{OW} and θ_{IW} are the central angle of each OW and IW winding, respectively, as shown in Fig. 6, to represent relationship between the geometries of cores and windings in MCT, and the leakage inductance of MCTs with different values of γ and simulated with 3-D FEA model. The simulation result and the curving fitting function are plotted in Fig. 9 with the parameter K_{MCT} defined as

$$K_{MCT}(\gamma)=\frac{L_{\sigma,FEA}}{L_{\sigma,Rogowski}} \tag{22}$$

to describe the ratio of simulated leakage inductance $L_{\sigma,FEA}$ and Rogowski-corrected leakage inductance. The curve fitting function is as

$$K_{MCT}(\gamma)=-0.0551\gamma^3+0.0152\gamma^2-0.01574\gamma+0.92 \tag{23}$$

with the sum of squares due to error (SSE) of 1.75×10^{-5}. K_{MCT} can be taken as 0.9 approximately for simplifying the calculation.

D. Thermal Considerations

With the increase of power density, the heat dissipation ability of the transformer may decrease significantly due to the lower surface area. To prevent the excessive high temperature rise and improve the reliability of MFT, the thermal management issues can be addressed using enhanced MFT system architecture, accurate thermal models to estimate the temperature distribution, and effective cooling approaches [41].

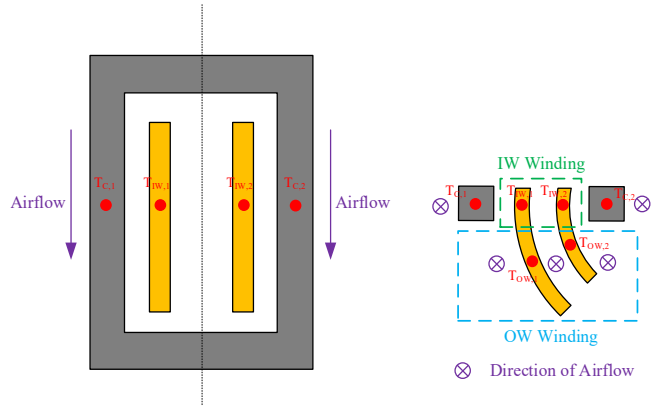

Fig. 10. Thermal models of MCT for IW winding, OW winding and the core.

As shown in Fig. 3, the split cores of MCT have more surface areas exposed to the air than the traditional shell type transformer to reduce the temperature rise due to the core loss. In addition, the space between two windings can be considered as an airflow channel for winding cooling. The thermal model of MCT is presented with two cases shown in Fig. 10, where the IW and OW windings are considered differently since the OW winding is cooled with forced air, thus the thermal coupling to the cores can be neglected. The core is divided to two parts horizontally with the same core loss, and the IW and OW windings are modeled for primary winding and secondary separately. The airflow cools the cores and the OW winding, and its direction is marked in Fig. 10. Based on the above analysis, the steady-state 2-D thermal network of MCT is proposed in Fig. 11, where the conduction, convection and radiation thermal resistances are defined as follows:

$$R_c=\frac{l}{\lambda A}, \tag{24}$$

$$R_{conv}=\frac{1}{\alpha_{conv}A}, \tag{25}$$

$$R_r=\frac{1}{\alpha_r A}, \tag{26}$$

where l is the thickness of the pad in the thermal flow direction, λ is the thermal conductivity of the material, α_{conv} is the convective heat transfer coefficient, and α_r is the radiative heat transfer coefficient. The approximate expressions for calculation of R_{conv} for different convection cases are from [42]. With the enhanced structure design for cooling, maximum average current density in the litz wire can be increased for further improved transformer power density by using the forced air cooling. The proposed thermal network model is verified with FEA simulation and experimental results shown in the followed sections.

E. Insulation Considerations

The gap between the windings and the distance between core and windings are the keys for the insulation design. The minimum value for insulation [21] can be calculated as

$$d_{min}=\frac{V_{iso}}{k_s E_{ins}}, \tag{27}$$

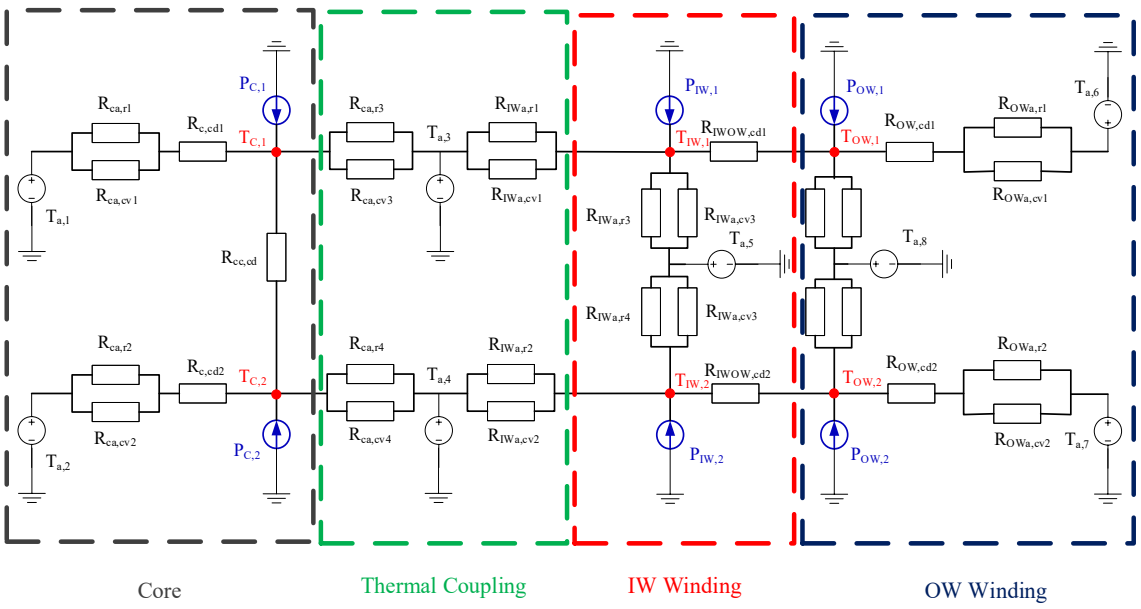

Fig. 11. Thermal network of MCT with the conduction, convection, and radiation thermal resistances. The hotspot nodes and the heat sources are marked with red and blue, respectively.

where k_s is the safety factor, E_{ins} is the dielectric strength of the insulation material, and V_{iso} is the insulation level, which is set as 10 kV according to IEEE Std C57.12.01™-2020 for the 1 kV/1 kV dry-type transformer [43]. The geometry requirements of the MCT are as

$$\min\left(D_\sigma, D_{w2c,h1}, D_{w2c,w1}, D_{w2c,h2}, D_{w2c,w2}\right) \geq d_{\min}, \quad (28)$$

where $D_{w2c,h1}$, $D_{w2c,w1}$, $D_{w2c,h2}$, and $D_{w2c,w2}$ are dimensions shown in Fig. 6. The (28) is used as one of the geometrical constrains for the MCT optimization.

III. Optimization Methodology and FEA Simulation

A. Pareto-front Optimization

Since the MFT with high efficiency η and high power density ρ is required for MEA power distribution, a multivariable and multi-objective optimization methodology for MCT has been developed based on the above MCT models. The constant, input, and output parameters for the optimization can be expressed as follows:

$$\boldsymbol{U} = \left[V_1, V_2, I_1, I_2, f, L_\sigma, L_m\right], \quad (29)$$

$$\boldsymbol{X} = \left[x_c, N_c, J_1, J_2, N_1, N_2, d_{str,1}, d_{str,2}\right], \quad (30)$$

$$\boldsymbol{Y} = \left[\eta, \rho, T_c, T_w\right], \quad (31)$$

where V_i, I_i, J_i, N_i and $d_{str,i}$ are the voltage, current, current density, number of turns and strand diameter of litz wire for each winding (primary winding for $i = 1$ and secondary winding for $i = 2$), respectively, x_c contains parameters of selected cores, which are the dimensions, effective cross-sectional area and Steinmetz coefficients from database, N_c is the number of cores, and T_c and T_w are the estimated peak temperatures of cores and windings, respectively. The flow chart of optimization algorithm is presented in Fig. 12, in which the database is setup with the parameters of available cores and litz wires, and the constrains filter the designs with core saturation, unsatisfied

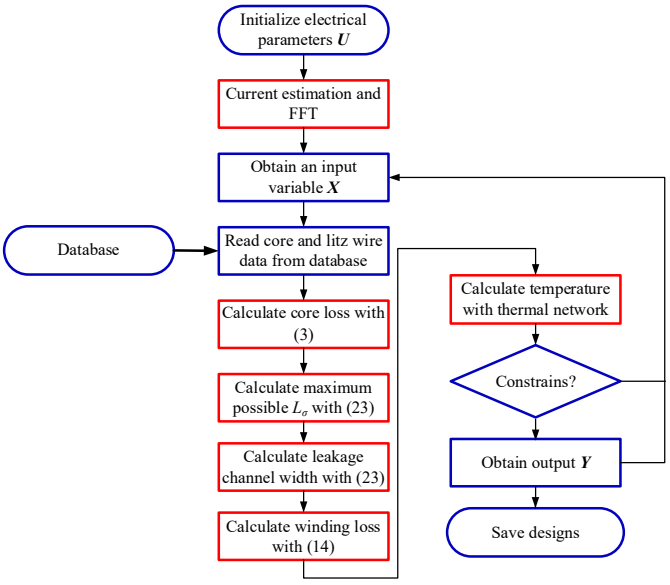

Fig. 12. The proposed optimization algorithm for MCT.

geometries of structure, insufficient leakage inductance, or overheat occurrence. The maximum possible leakage inductance is calculated first to check the availability of each design, and then the accurate length of winding gap is calculated for obtaining required leakage inductance. The current waveform is estimated for FFT. The geometries of the windings are controlled with the leakage inductance control and used for the winding loss calculation. The loop proceeds for each combination of input variables, and the parameters of all available design candidates are saved for the subsequent comparisons of efficiency and power density.

B. Key Parameters and 3-D Model of 100 kW MCT Design

The proposed optimization methodology is performed for the design of a 100 kW, 50 kHz, 1 kV/1 kV MCT with 10 μH

Table I
KEY PARAMETERS OF THE OPTIMAL100 KW MCT DESIGN

Parameter	Value
Power	100 kW
Voltage	1 kV/1 kV
Frequency	50 kHz
Leakage Inductance	10 μH
Core	Magnetics 0P49930UC × 10
Litz Wire	AWG 38 × 2500
Turns-ratio	8:8

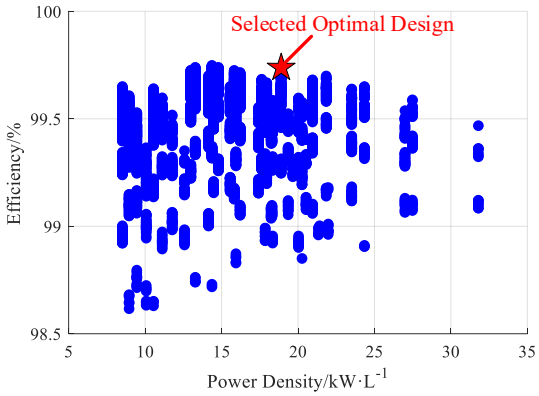

Fig. 13. Result of Pareto optimization for the 100 kW MCT design. The off-the-shelf ferrite cores and litz wires are listed as the candidate solutions.

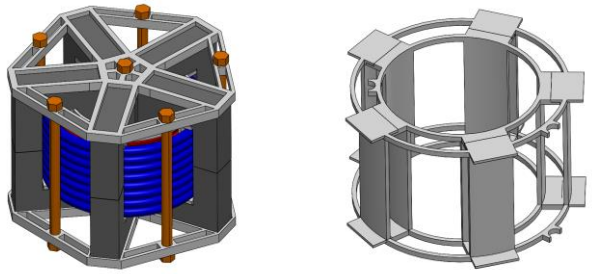

(a) (b)

Fig. 14. 3-D model of (a) the designed MCT and (b) 3-D printed bobbin with airflow channel for winding cooling.

leakage inductance for DAB converter. The candidate cores are off-the-shelf ferrite cores, and the maximum allowable temperature for core and windings are 100℃ and 150℃, respectively. The optimization result is shown in Fig. 13, and the key parameters of the selected MCT design with the highest efficiency are summarized in Table I. The 3-D model of the optimal MCT design is shown in Fig. 14(a), in which two bases are placed on the top and bottom of the transformer for stabilizing the structure. The slots of the bases are designed for improving heat dissipation on the surfaces of cores. The detailed 3-D model of bobbin in the MCT is shown in Fig. 14(b), which is designed with concerns as decreasing the thermal coupling between the windings and cores, provide path for airflow, controlling the leakage inductance, and ensuring sufficient dielectric strength for insulation consideration. Differ from a complete cylinder, the bobbin is also designed with slots, which increases the area of winding exposed to the airflow.

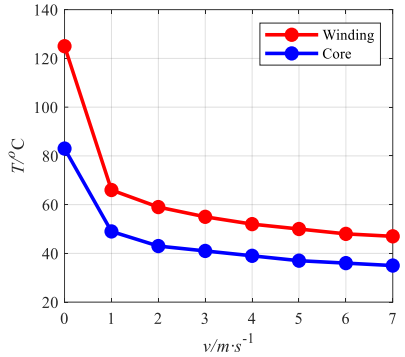

Fig. 15. The simulated temperature of hotspots on the windings and the core under different airflow velocity.

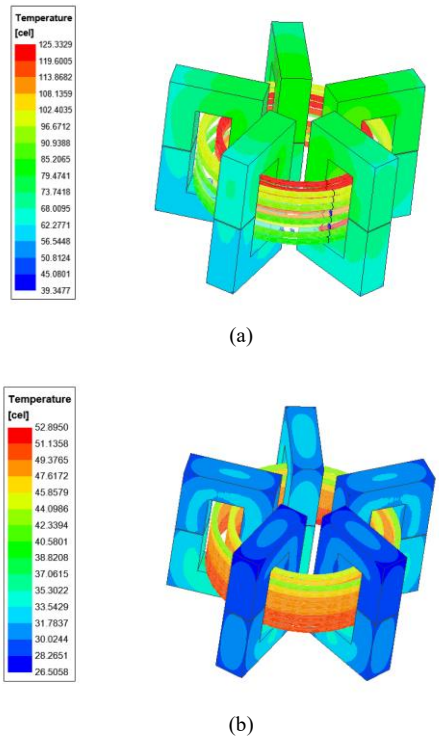

Fig. 16. The temperature distribution of the MCT under (a) natural convection and (b) v = 5 m/s forced air convection. The airflow channel provides sufficient path for air cooling.

TABLE II
TRANSFORMER INSULATION COMPONENTS

	Function	Dielectric Strength	Dielectric Constant
Air	Main Insulation	3 kV/mm	1
Polyimide (PI) Tape	Litz Wire Jacket and Winding Insulation	197 kV/mm	3.0
Acrylonitrile Butadiene Styrene (ABS)	Bobbin	18 kV/mm	3.1

C. *Design Validation using FEA Simulation*

To verify the thermal design of the MCT, the steady-state temperature distributions for both natural convection and forced air convection are simulated by Ansys/Icepak. The hotspot temperature on the core and windings with variable airflow velocity are illustrated in Fig. 15. The temperature distributions of the MCT for different airflow speeds, i.e., v = 0 and v = 5

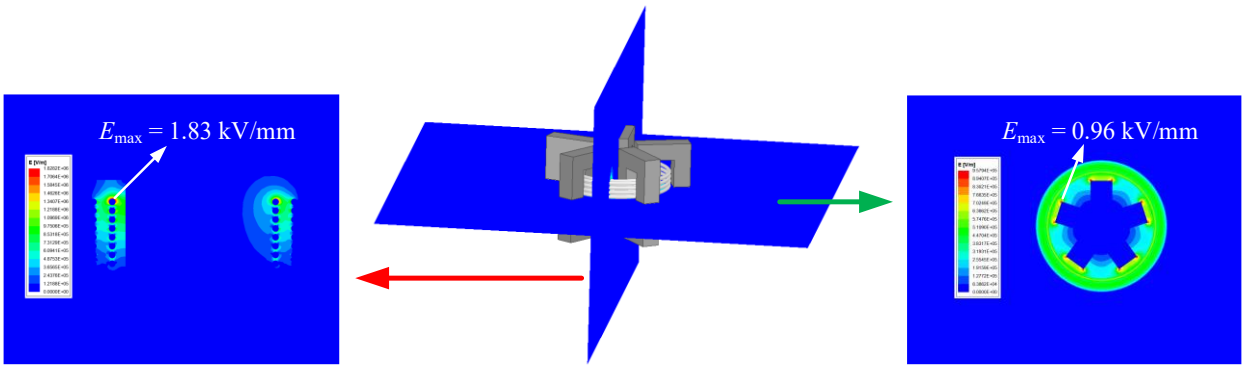

Fig. 17. The simulated electrical field distribution of front view (left) and top view (right).

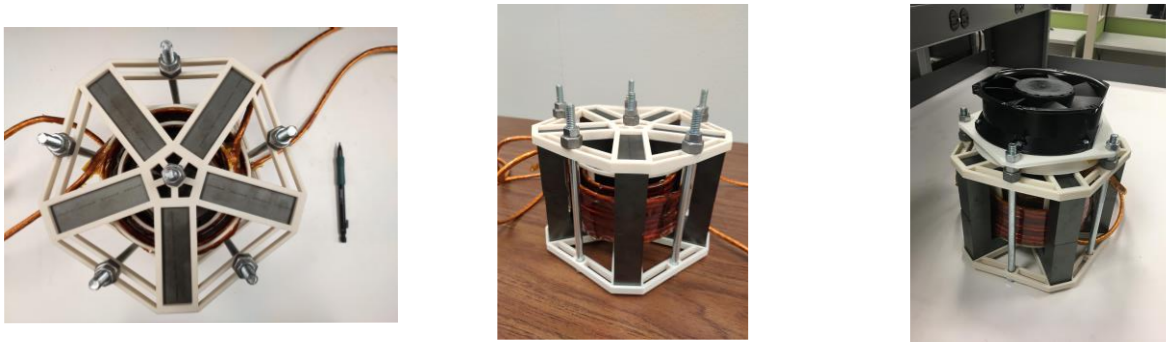

(a) (b) (c)

Fig. 18. The prototype of the MCT. (a) Top view and size comparison with a ballpoint pen. (b) Front view and (c) with fan installed on top.

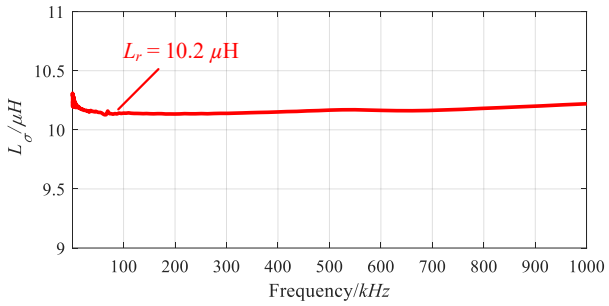

(a)

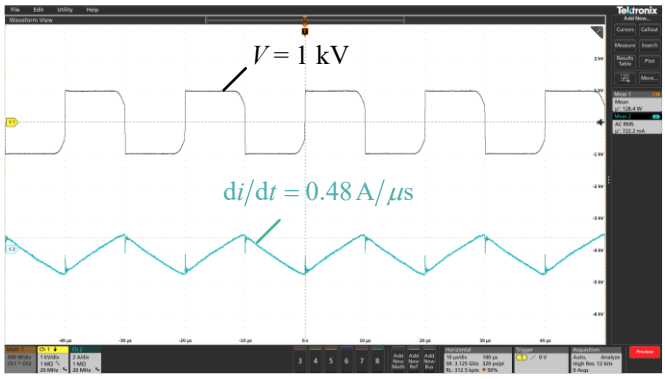

(b)

Fig. 19. (a) The measured value of leakage inductance with the frequency swept from 1 kHz to 500 kHz. (b) The waveforms of OC test to measure the magnetizing inductance and core loss.

m/s, are shown in Fig. 16. The temperature rise of the high current windings under natural convection is acceptable and can be further reduced by forced air convection with the designed airflow channel.

The voltage insulation capability of the 100 kW MCT design is verified by the simulated electric field strength E. With the potential of core is set to 0 and the isolation level of primary and secondary winding is distributed evenly on each turn, a 10 kV voltage is applied between the primary and secondary windings, and the simulation result of electric field distribution with 3-D electrostatic simulation as Fig. 17 [43]. The peak E occurs around the turn with maximum voltage applied, and its value is 1.83 kV/mm, which is lower than the breakdown field strengths of all the used insulation components listed in Table II.

IV. Prototype and Experimental Verification

The top view and front view of prototype of MCT are shown in Fig. 18(a) and (b). The outer diameter of selected round litz wire is 6.5 mm for both windings. The bases and bobbin are all made by 3-D printing technology with ABS [44]. A fan is installed on the MCT for forced air convection test as shown in Fig. 18(c). The fan is selected with 172 mm diameter, which is large enough to cover the airflow channel. The air velocity of the fan is 4.16 m/s (205 cfm), and the power consumption is 12 W. The power densities of the MCT without and with fan are 17.7 kW/L and 14.2 kW/L, respectively.

A. Electrical Parameter Measurement

The leakage inductance L_σ and the magnetizing inductance L_m should be measured before the full power operation test. The

plot of L_σ measured by vector network analyzer Bode 100 with the sweep frequency from 1 kHz to 500 kHz are shown in Fig. 19(a). As can be seen that the value of L_σ maintains as 10.2 μH in a wide range, which matches the design requirement. The value of L_m is measured with the open circuit (OC) test, and the waveforms are shown in Fig. 19(b). Based on the measured data of voltage and di/dt, L_m reaches 2.1 mH, which demonstrates a ratio of L_m and L_σ over 200. It is a reasonable value since L_m should be designed much larger than L_σ to reduce the magnetizing current for the DAB converter [12]. In addition, core loss can be measured as 128 W with OC test.

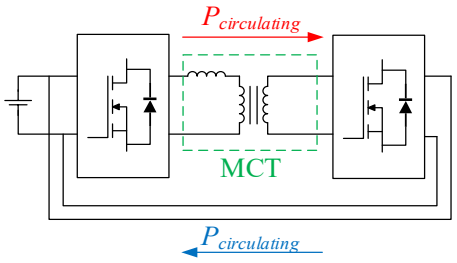

(a)

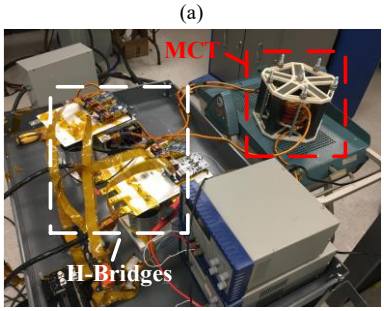

(b)

Fig. 20. (a) The schematic and (b) test setup of pump-back test for the MCT operation.

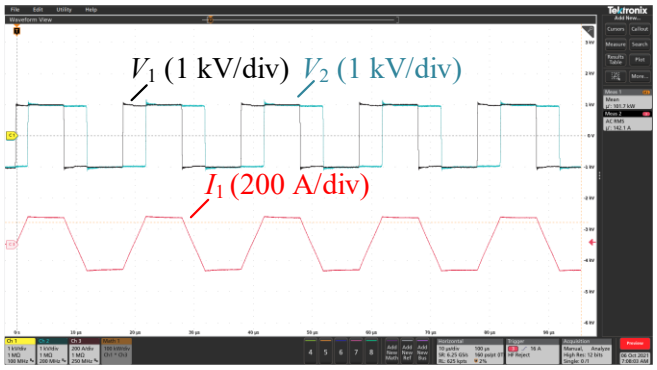

Fig. 21. The measured voltage and current waveforms for the MCT at 100 kW.

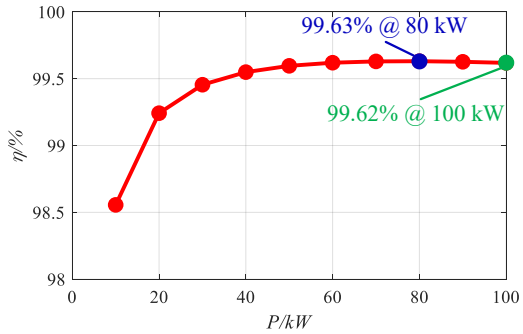

Fig. 22. The efficiency of the MCT at different power level.

B. Pump-back Power Test

To evaluate the performance of the MCT prototype, a pump-back test setup with two H-bridges sharing the common DC-link of together is developed. The schematic and setup are shown in Fig. 20. The H-bridges are designed with 1700 V SiC MOSFET half-bridge modules and a high current carrying-capacity busbar with low stray inductance [45]. One of the advantages of pump-back test is that the total power loss of the system is equal to the power delivered from the DC power

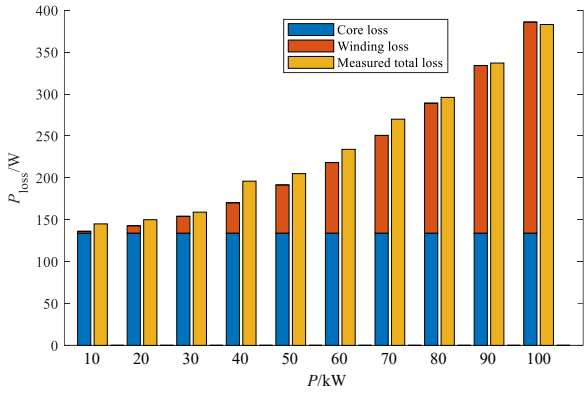

Fig. 23. The comparison of estimated losses from the analytical models and measured loss.

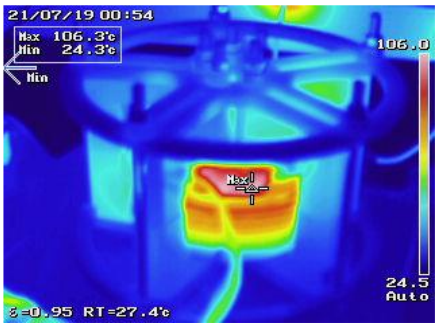

(a)

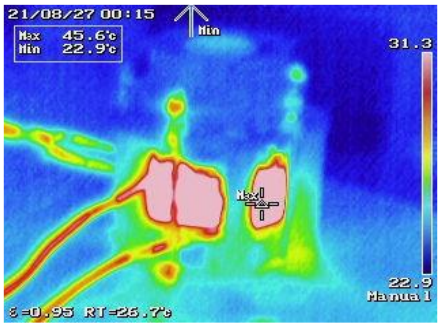

(b)

Fig. 24. The thermal images for the MCT in steady state at 100 kW (a) without fan and (b) with fan.

supply because of the absence of the load. The power loss of the MCT is calculated as

$$P_{\mathrm{MCT}} = P_{\mathrm{total}} - P_{\mathrm{sw}} - P_{\mathrm{con}}\,, \tag{32}$$

where P_{total} is total power loss obtained from the power supply, P_{sw} and P_{con} are the switching loss and conduction loss of the switches, respectively. P_{sw} and P_{con} are modeled with the curve fitting tool based on the measured loss data from double pulse

test (DPT) [45]. The SPS modulation is adapted in this test, and the phase shift φ is expressed as

$$\varphi = \varphi_o + \varphi_{dt}, \tag{33}$$

where φ_o is the phase shift derived from the basic power model of DAB converter

$$P = \frac{nV_1V_2}{2\pi^2 f_s L_\sigma}\varphi_o(\pi - \varphi_o) \tag{34}$$

and φ_{dt} is the phase shift compensate for the dead-time effect [46]. The waveforms of voltage and current at full power operation are presented in Fig. 21, and the efficiency curve of

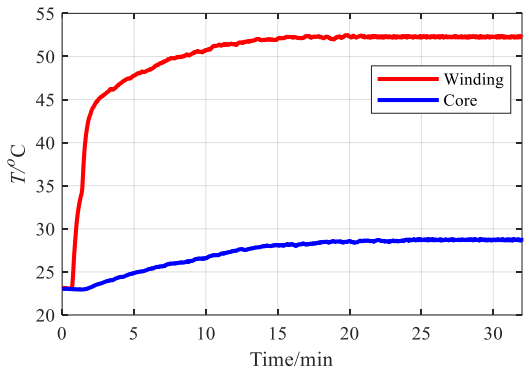

Fig. 25. The hotspot temperature rise profile measured by thermocouple during full power operation. The stable hotspot temperature of the windings and the core are 53°C and 29°C, respectively.

the MCT for different power level is plotted in Fig. 22 by varying the phase shift. The efficiency of the MCT reaches the peak value of 99.63% at 80 kW, and value of 99.62% at the rated power. The estimated core and winding losses from the analytical models are compared with the measured total loss in Fig. 23, which verifies the accuracy of proposed models and optimization methodology.

C. Thermal Performance Characterization

The thermal performances of the MCT for natural convection and forced air convection are both evaluated under the pump-back test. The both tests run for over 30 minutes at the full power operation to ensure the steady-state temperature rise is reached. The thermal camera images of the transformer are shown in Fig. 24, which illustrate the thermal distribution of the MCT matching with the thermal models. The peak winding temperature with forced air convection is 45.6°C, which is much lower than the 106.3°C using natural convection. The accurate hotspot temperature of the MCT with fan is measured with National Instruments cDAQ-9174 chassis and NI-9213 thermocouple input module as shown in Fig. 25. The thermocouples are placed at the maximum temperature location identified via the thermal camera. It takes about 15 minutes for the MCT to reach the steady state, and the result of hotspot temperature verifies the proposed thermal models.

V. Conclusion

The rapid development of MEA requires the power conversion and distribution systems with both high power ratings and high power density. In this paper, a detailed process of designing a high power MCT for MEA power distribution is discussed. Comprehensive electromagnetic and thermal models of MCT are introduced. The detailed considerations for core and litz wire selection and thermal management design are proposed. An optimization methodology for MCT is presented for high efficiency, high power density transformer design. A 100 kW, 50 kHz MCT prototype for high-power DAB converter has been developed based on the optimal result. Electrical parameters, such as the leakage and magnetizing inductance, are measured. The full power operation of the DAB prototype is demonstrated using a pump-back test. The steady-state temperature rises of the prototype with both natural convection and forced air convection are measured to verify the thermal model of MCT. The efficiency curve for variable power level is presented with a measured peak efficiency at 99.63%. The successful test results prove the application of MCT on the application and provide the possibility of higher power and high frequency transformer design in the future.

References

[1] B. Sarlioglu and C. T. Morris, "More electric aircraft: Review, challenges, and opportunities for commercial transport aircraft," in *IEEE Trans. Transport. Electrific.*, vol. 1, no. 1, pp. 54-64, Jun. 2015.

[2] V. Madonna, P. Giangrande and M. Galea, "Electrical power generation in aircraft: review, challenges, and opportunities," in *IEEE Trans. Transport. Electrific.*, vol. 4, no. 3, pp. 646-659, Sept. 2018.

[3] J. Wang et al., "Characterization, modeling, and application of 10-kV SiC MOSFET," in *IEEE Trans. Electron Devices*, vol. 55, no. 8, pp. 1798-1806, Aug. 2008.

[4] K. Vechalapu, S. Bhattacharya, E. Van Brunt, S. Ryu, D. Grider, and J. W. Palmour, "Comparative evaluation of 15-kV SiC MOSFET and 15-kV SiC IGBT for medium-voltage converter under the same dv/dt conditions," in *IEEE J. Emerg. Sel. Topics Power Electron.*, vol. 5, no. 1, pp. 469-489, Mar. 2017.

[5] S. Zhao, Q. Li, F. C. Lee, and B. Li, "High-frequency transformer design for modular power conversion from medium-voltage AC to 400 VDC," in *IEEE Trans. Power Electron*., vol. 33, no. 9, pp. 7545-7557, Sept. 2018.

[6] G. Zhu et al., "Wireless power transformation for data centers and medium voltage applications," in *Proc. IEEE. Appl. Power Electron. Conf. Expo.*, 2020, pp. 798-804.

[7] X. Zhao, J. Hu, L. Ravi, D. Dong, and R. Burgos, "Planar common-mode EMI filter design and optimization in a 100-kW SiC-based generator-rectifier system for high-altitude operation, " in *Pro. IEEE. Energy Convers. Congr. Expo.* (*ECCE*), 2021, pp. 3555-3562.

[8] X. She, A. Q. Huang, and R. Burgos, "Review of solid-state transformer technologies and their application in power distribution systems," in *IEEE J. Emerg. Sel. Topics Power Electron.*, vol. 1, no. 3, pp. 186-198, Sept. 2013.

[9] C. G. Dincan et al., "Design of a high-power resonant converter for DC wind turbines," in *IEEE Trans. Power Electron*., vol. 34, no. 7, pp. 6136-6154, Jul. 2019.

[10] C. Gu et al., "A multiport power conversion system for the more electric aircraft," in *IEEE Trans. Transport. Electrific.*, vol. 6, no. 4, pp. 1707-1720, Dec. 2020.

[11] G. Buticchi, L. Costa, and M. Liserre, "Improving system efficiency for the more electric aircraft: A look at DC/DC converters for the avionic onboard DC microgrid," in *IEEE Ind Electron. Mag.*, vol. 11, no. 3, pp. 26-36, Sept. 2017.

[12] J. Chen, C. Wang, and J. Chen, "Investigation on the selection of electric power system architecture for future more electric aircraft," in *IEEE Trans. Transport. Electrific.*, vol. 4, no. 2, pp. 563-576, Jun. 2018.

[13] B. Zhao, Q. Song, W. Liu, and Y. Sun, "Overview of dual-active-bridge isolated bidirectional DC–DC converter for high-frequency-link power-conversion system," in *IEEE Trans. Power Electron*., vol. 29, no. 8, pp. 4091-4106, Aug. 2014.

[14] G. Oggier, G. O. García, and A. R. Oliva, "Modulation strategy to operate the dual active bridge DC-DC converter under soft switching

in the whole operating range," in *IEEE Trans. Power Electron*., vol. 26, no. 4, pp. 1228-1236, Apr. 2011.
[15] X. Margueron, J. P. Keradec, and D. Magot, "Analytical calculation of static leakage inductances of HF transformers using PEEC formulas," *IEEE Trans. Ind. Appl.*, vol. 43, no. 4, pp. 884–892, Jul./Aug. 2007.
[16] M. Lambert, M. Martinez-Duro, J. Mahseredjian, F. De Leon, and F. Sirois, "Transformer leakage flux models for electromagnetic transients: Critical review and validation of a new model," *IEEE Trans. Power Del.*, vol. 29, no. 5, pp. 2180–2188, Oct. 2014.
[17] X. Margueron, A. Besri, P. O. Jeannin, J. P. Keradec, and G. Parent, "Complete analytical calculation of static leakage parameters: A step toward HF transformer optimization," *IEEE Trans. Ind. Appl.*, vol. 46, no. 3, pp. 1055–1063, May/Jun. 2010.
[18] R. Schlesinger and J. Biela, "Comparison of analytical models of transformer leakage inductance: Accuracy versus computational effort," in *IEEE Trans. Power Electron*., vol. 36, no. 1, pp. 146-156, Jan. 2021.
[19] D. Rothmund, T. Guillod, D. Bortis, and J. W. Kolar, "99% efficient 10 kV SiC-based 7 kV/400 V DC transformer for future data centers," in *IEEE J. Emerg. Sel. Topics Power Electron.*, vol. 7, no. 2, pp. 753-767, Jun. 2019.
[20] M. Mogorovic and D. Dujic, "100 kW, 10 kHz medium-frequency transformer design optimization and experimental verification," in *IEEE Trans. Power Electron*., vol. 34, no. 2, pp. 1696-1708, Feb. 2019.
[21] B. Chen, X. Liang and N. Wan, "Design methodology for inductor-integrated litz-wired high-power medium-frequency transformer with the nanocrystalline core material for isolated DC-link stage of solid-state transformer," in *IEEE Trans. Power Electron*., vol. 35, no. 11, pp. 11557-11573, Nov. 2020.
[22] Z. Guo, R. Yu, W. Xu, X. Feng, and A. Q. Huang, "Design and optimization of a 200-kW medium-frequency transformer for medium-voltage SiC PV inverters," in *IEEE Trans. Power Electron*., vol. 36, no. 9, pp. 10548-10560, Sept. 2021.
[23] G. Ortiz, M. G. Leibl, J. E. Huber, and J. W. Kolar, "Design and experimental testing of a resonant DC–DC converter for solid-state transformers," in *IEEE Trans. Power Electron*., vol. 32, no. 10, pp. 7534-7542, Oct. 2017.
[24] D. Rothmund, G. Ortiz, T. Guillod, and J. W. Kolar, "10kV SiC-based isolated DC-DC converter for medium voltage-connected solid-state transformers," in *Proc. IEEE. Appl. Power Electron. Conf. Expo.*, 2015, pp. 1096-1103.
[25] W. G. Hurley and W. H. Woelfle, *Transformers and Inductors for Power Electronics—Theory, Design and Applications.* New York, NY, USA: Wiley, 2013.
[26] W. Shen, F. Wang, D. Boroyevich, and C. W. Tipton IV, "High-Density nanocrystalline core transformer for high-power high-frequency resonant converter," in *IEEE Trans. Ind. Appl.*, vol. 44, no. 1, pp. 213-222, Jan.-Feb. 2008.
[27] S. Somkun, T. Sato, V. Chunkag, A. Pannawan, P. Nunocha, and T. Suriwong, "Performance comparison of ferrite and nanocrystalline cores for medium-frequency transformer of dual active bridge DC-DC converter," *Energies*, vol. 14, no. 9, p. 2407, Apr. 2021.
[28] W. A. Roshen, "A practical, accurate and very general core loss model for nonsinusoidal Waveforms," in *IEEE Trans. Power Electron*., vol. 22, no. 1, pp. 30-40, Jan. 2007.
[29] C. P. Steinmetz, "On the law of hysteresis," *Proc. IEEE*, vol. 72, no. 2, pp. 197-221, Feb. 1984.
[30] K. Venkatachalam, C. R. Sullivan, T. Abdallah, and H. Tacca, "Accurate prediction of ferrite core loss with nonsinusoidal waveforms using only Steinmetz parameters," in *Proc. IEEE Workshop Comput. Power Electron.*, Jun. 2002, pp. 36-41.
[31] J. Reinert, A. Brockmeyer, and R. W. A. A. De Doncker, "Calculation of losses in ferro- and ferrimagnetic materials based on the modified Steinmetz equation," in *IEEE Trans. Ind. Appl.*, vol. 37, no. 4, pp. 1055-1061, Jul.-Aug. 2001.
[32] J. Muhlethaler, J. Biela, J. W. Kolar, and A. Ecklebe, "Improved core-loss calculation for magnetic components employed in power electronic systems," in *IEEE Trans. Power Electron*., vol. 27, no. 2, pp. 964-973, Feb. 2012.
[33] M. A. Bahmani, T. Thiringer, and M. Kharezy, "Design methodology and optimization of a medium-frequency transformer for high-power DC–DC applications," in *IEEE Trans. Ind. Appl.*, vol. 52, no. 5, pp. 4225-4233, Sept.-Oct. 2016.
[34] P. L. Dowell, "Effects of eddy currents in transformer windings," *Proc. Inst. Electr. Eng.*, vol. 113, no. 8, pp. 1387–1394, Aug. 1966.
[35] R. P. Wojda and M. K. Kazimierczuk, "Winding resistance and power loss of inductors with litz and solid-round wires," in *IEEE Trans. Ind. Appl.*, vol. 54, no. 4, pp. 3548-3557, Jul.-Aug. 2018.
[36] Z. Zhao, Y. Wu, X. Du, and Y. Zhao, "Design and optimization of the high frequency transformer for 100 kW CLLC converter, " in *Proc. IEEE. Appl. Power Electron. Conf. Expo.* (*APEC*), 2021, pp. 1709-1716.
[37] Z. Ouyang, J. Zhang, and W. G. Hurley, "Calculation of leakage inductance for high-frequency transformers," in *IEEE Trans. Power Electron*., vol. 30, no. 10, pp. 5769-5775, Oct. 2015.
[38] Z. Ouyang and M. A. E. Andersen, "Overview of planar magnetic technology—Fundamental properties," in *IEEE Trans. Power Electron*., vol. 29, no. 9, pp. 4888-4900, Sept. 2014.
[39] S. V. Kulkarni and S. A. Khaparde, *Transformer Engineering: Design and Practice*. New York, NY, USA: Marcel Dekker, Inc., 2004. [Online]. Available: https://dotorresg.files.wordpress.com /2011/12/4-transformer- engineering -design-and-practice-s-v-kulkarnis-a-khaparde2004.pdf
[40] M. Mogorovic and D. Dujic, "Medium frequency transformer leakage inductance modeling and experimental verification," *IEEE Energy Convers. Congr. Expo.*, 2017, pp. 419-424.
[41] C. Zhao et al., "Power electronic traction transformer—medium voltage prototype," in *IEEE Trans. Ind. Electron.*, vol. 61, no. 7, pp. 3257-3268, Jul. 2014.
[42] Bergman, Theodore L., et al. *Fundamentals of heat and mass transfer.* John Wiley & Sons, 2011.
[43] IEEE Standard for General Requirements for Dry-Type Distribution and Power Transformers, in IEEE Std C57.12.01-2020 (Revision of IEEE Std C57.12.01-2015), 2015.
[44] CROW. *Acrylonitrile-Butadiene-Styrene* (*ABS*). [Online]. Available: https://polymerdatabase.com /Commercial%20Polymers/ABS.html. [Accessed Oct. 14, 2021].
[45] Y. Wu et al., "A 150-kW 99% efficient all silicon carbide triple-active-bridge converter for solar-plus-storage systems," in *IEEE J. Emerg. Sel. Topics Power Electron.*, doi: 10.1109/JESTPE.202 0.3044572.
[46] B. Zhao, Q. Song, W. Liu, and Y. Sun, "Dead-time effect of the high-frequency isolated bidirectional full-bridge DC–DC converter: Comprehensive theoretical analysis and experimental verification," in *IEEE Trans. Power Electron*., vol. 29, no. 4, pp. 1667-1680, Apr. 2014.

Zhe Zhao (Graduate Student Member, IEEE) received the B.S. in electrical engineering from Huazhong University of Science and Technology, Wuhan, China, in 2016, and the M.S. degree in electrical engineering from Arizona State University, Tempe, USA, in 2017. He is currently working toward the Ph.D. degree with the Department of Electrical Engineering, University of Arkansas, Fayetteville, AR, USA.

In 2019, he was a Graduate Intern with the Enabling Technologies Group, Schlumberger, Sugar Land, TX, USA. His research interests include power converter control and power electronics transformer design.

Yuheng Wu (Student Member, IEEE) received the B.E. and M.E. degrees in automation from Nanjing University of Aeronautics and Astronautics, Nanjing, China in 2015 and 2018, respectively. He was a Summer Intern with John Deere Electronic Solutions (JDES), Fargo, ND, USA, in 2020 and 2021. He is currently working towards the Ph.D. degree in electrical engineering with the Department of Electrical Engineering, University of Arkansas, Fayetteville, United States.

His research interests are in the field of control theory with applications to power electronics and ac motor drivers.

Fei Diao (Graduate Student Member, IEEE) received the B.E. and M.E. degrees in electrical engineering from Southwest Jiaotong University, Chengdu, China, in 2015 and 2018, respectively. He is currently working toward the Ph.D. degree in electrical engineering with Department of Electrical Engineering, University of Arkansas, Fayetteville, AR, USA. In 2020 and 2021, he was a Summer Intern with Eaton Corporation, Menomonee Falls, WI, USA.

His main research interests include modulation and control of power converters, wide bandgap (WBG) power device applications.

Nan Lin (Graduate Student Member, IEEE) received the B.S. degree in electrical engineering from Wuhan University, Wuhan, China, in 2015, and the M.S. degree in electrical engineering from Zhejiang University, Hangzhou, China, in 2018. He is currently working toward the Ph.D. degree with the Department of Electrical Engineering, University of Arkansas, Fayetteville, AR, USA.

His research interests include bidirectional dc-dc converter and motor control.

Xinyuan Du (Student Member, IEEE) received the B.S. degree in electrical engineering from Chongqing University, Chongqing, China, in 2015, and the M.S. degree from the Huazhong University of Science and Technology, Wuhan, China, in 2018. He is currently pursuing the Ph.D. degree with University of Arkansas, Fayetteville, AR, USA.

His research interests include medium-voltage converters, high frequency resonant converters and magnetics.

Yue Zhao (Senior Member, IEEE) received a B.S. degree in electrical engineering from Beijing University of Aeronautics and Astronautics, Beijing, China, in 2010, and a Ph.D. degree in electrical engineering from the University of Nebraska-Lincoln, Lincoln, USA, in 2014.

He was an Assistant Professor in the Department of Electrical and Computer Engineering at the Virginia Commonwealth University, Richmond, USA, in 2014-2015. Since August 2015, he has been with the University of Arkansas, Fayetteville, USA, where he is currently an Associate Professor in the Department of Electrical Engineering. He also serves as the site director for National Science Foundation (NSF) Center for GRid-connected Advanced Power Electronic Systems (GRAPES). His current research interests include electric machines and drives, power electronics, and renewable energy systems. He has 4 U.S. patents granted and co-authored more than 100 papers in refereed journals and international conference proceedings.

Dr. Zhao is an Associated Editor of the IEEE Transactions on Industry Applications and IEEE Open Journal of Power Electronics. He was a recipient of 2018 U.S. National Science Foundation CAREER Award, the 2020 IEEE Industry Applications Society Andrew W. Smith Outstanding Young Member Achievement Award and the 2020 UA College of Engineering Dean's Award of Excellence.

Guangqi Zhu (Member, IEEE) received the B.S. and M.S. degrees from Harbin Institute of Technology, Harbin, China, in 2011 and 2013, respectively. He received the Ph.D. degree from the University of Wisconsin - Madison, Madison, WI, USA, in 2018. He works as a Specialist Engineer - Power Conversion at Eaton Research Labs, Menomonee Falls, WI. His research interests include wireless power transfer, high frequency magnetics design, and high frequency resonant converter design.